CHAPTER 2

Growth of Laser Diode Structure using MOVPE

2. Growth of Laser Diode Structure using MOVPE

Fabrication of high-power laser diode requires multilayered semiconductor material structure of excellent electrical and optical quality, which is determined by the epitaxial growth. This chapter discusses issues related to the epitaxial growth of semiconductor materials and optimization of layer-sequences that form the foundation for high-power laser diodes. Various epitaxial growth techniques are discussed briefly with emphasis on metal-organic vapor phase epitaxy (MOVPE). X-ray and optical characterization techniques utilized to study the MOVPE grown semiconductor materials are discussed. The sequential growth of a complete laser diode structure with layers of controlled thicknesses, composition and doping profiles, optimized to make the laser diode emit in the red portion of the spectrum, is presented.

2.1 Introduction

Laser diodes have been realized over a wide range of lasing wavelength with a variety of material systems. The advancements in technological breakthroughs, especially in crystal growth techniques, have brought down the threshold current densities of laser diodes by more than three orders of magnitude. Evolution of laser diodes, from the early homojunction lasers, through double-heterojunction (DH) laser structures that resulted from the improvement in liquid phase epitaxy (LPE) in the early 70's, has reached to the development of quantum-well (QW) and quantum-dot (QD) lasers, which have been realized by the progress in growth technologies like molecular beam epitaxy (MBE) and metal-organic vapor phase epitaxy (MOVPE).

Most high-power laser diodes today are based on III-V semiconductor QW structure having just a few nanometer thick active layer with precisely controlled composition and good homogeneity. The light, generated by the band-to-band recombination in the QW active region, is transversely confined by means of waveguide and cladding layers. These layers are much thicker, a few micrometer, and have to be grown at a reasonable growth rate in order to ensure the economic feasibility of the process. All of these have to be achieved while maintaining high crystalline quality with

minimal defects, and with a tight control of the doping profile, requiring optimized epitaxial growth conditions for the individual layers of the laser structure.

The lasing wavelength of the laser diode is determined by the material systems employed and covers a broad spectrum to justify various applications. InP based materials, GaInAs(P) and (Al)GaInAs, cover the wavelength range of 1100 nm to 1900 nm which is important for optical fiber transmission around 1300 nm and 1550 nm [1,2]. Although high optical power is not necessary for optical communication, it may serve the other emerging applications such as range-finding, free-space communications, and marking using this wavelength range. The wavelength range from around 700 nm to 1060 nm is covered by GaAs-based devices with various III-V combinations. Red lasers in the range of 630-690 nm are achieved with GaInP QWs. Emission in blue-green region has been achieved using II-VI compounds, like ZnMgSSe-based systems [3], which is lattice-matched to the GaAs substrates. GaN-based material systems, though in an early stage of development, offer promising possibilities for laser diodes in the UV region with the blue laser diodes operating in continuous-wave (CW) mode at room-temperature have already been reported [4].

2.2 Epitaxial Growth of Semiconductor Materials

Epitaxy stands for the regular oriented growth of a single crystal layer with controlled thickness and doping, over a similar single crystal, called the substrate. Epitaxial techniques are now exploited to realize junctions, ultra-thin layers, and quantum structures, with unprecedented control over thickness, purity, and doping profile.

For epitaxial growth, matching of symmetry between the crystal planes of the substrate and the epitaxial layer is crucial. For good quality thick epitaxial layers, the lattice constants of the substrate and the epitaxial layer must be well-matched. Selection of epi-layer composition to achieve lattice-matching, while providing good carrier and optical confinement, is particularly important for the heterostructures used in laser didoes. The lattice mismatch, i.e. the difference between the lattice constants of the substrate and the epitaxial layer, should not exceed a critical limit. The large value of lattice mismatch usually results in the generation of dislocations and defects, degrading the quality of the

grown layer. The lattice-mismatch also determines the onset of three-dimensional (3D) growth-mode, commonly known as the Stranski-Krastanov growth-mode [5].

While exact lattice matching is required for thick epilayers, growth of very high quality strained epitaxial layers within a critical value of thickness (h_c) is possible with the modern growth techniques. The strained layer gives rise to several interesting properties. These include change in the effective masses of electrons and holes and the shift in the energy of band-edges relative to each other. If the strain in the epitaxial layer is coherent, the lattice constant of the layer in a direction parallel to the interface is forced to be equal to the lattice constant of the substrate. The lattice constant of the layer perpendicular to the interface will either expand or contract depending upon the lattice-mismatch between the substrate and the layer. If lattice constant of the layer is larger than that of the substrate then strain incorporated in the layer is called 'compressive strain', wherein the lattice constant in the direction parallel to the interface is forced to shrink while that perpendicular to the interface expands. Tensile strain arises, if lattice constant of the layer is smaller than that of the substrate. In this case, lattice constant of the layer parallel to the interface expands while that perpendicular to the interface shrinks. These two cases are depicted in figure 2.1 [6,7,8].

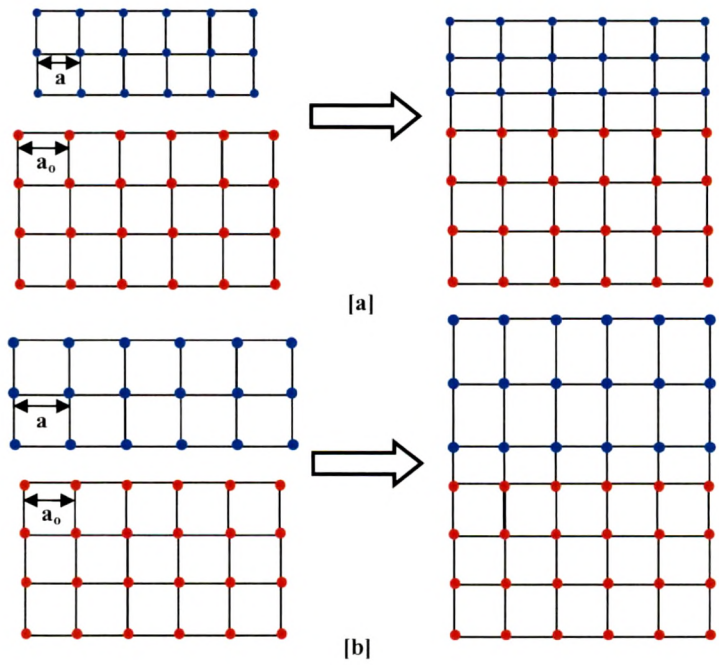

Figure 2.1: Schematic diagram showing (a) biaxial compressive strain (b) biaxial tensile strain.

After a critical value of the layer thickness, the layer cannot accommodate the built-in stress generated by the strain and relaxes to its original lattice constant. Such a relaxed layer shows much weaker relationship of the orientations of planes with the substrate.

The biaxial strain modifies the band structure of the semiconductor layer. The modification in band structure due to strain is illustrated in figure 2.2.

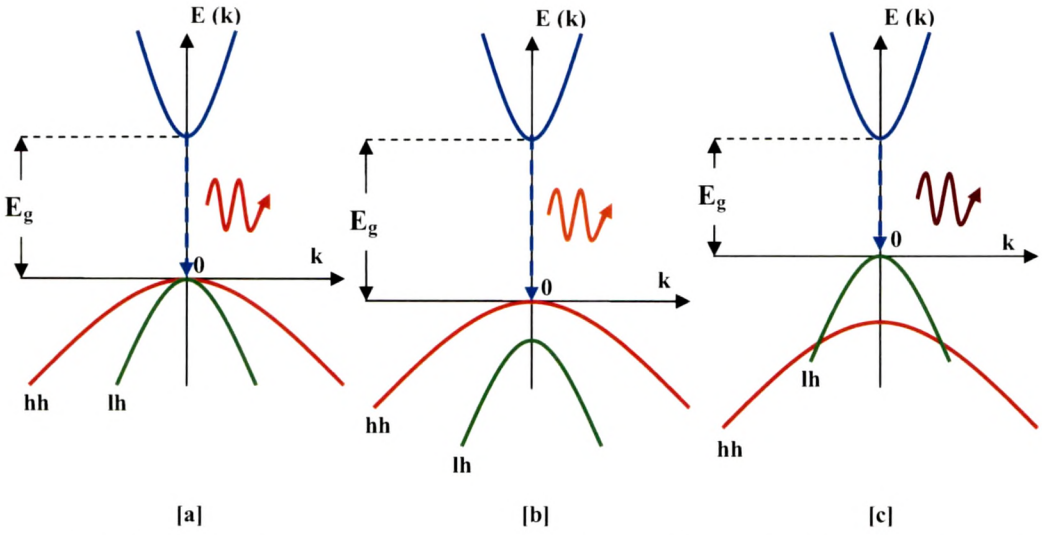

Figure 2.2: Schematic E-k diagram for [a] an unstrained direct bandgap semiconductor [b] semiconductor under biaxial compression [c] semiconductor under biaxial tension.

The effect of biaxial strain is stronger on the valence band structure since the top of the valence band is doubly degenerate. The energy difference between the conduction band and the valence band at k = 0 is given by [6],

$$\Delta E_{hh} = -2df\frac{C_{11}-C_{12}}{C_{11}} + bf\frac{C_{11}+2C_{12}}{C_{11}} \tag{2.1}$$

$$\Delta E_{lh} = -2df\frac{C_{11}-C_{12}}{C_{11}} - bf\frac{C_{11}+2C_{12}}{C_{11}} \tag{2.2}$$

where, ΔE_{hh} and ΔE_{lh} are the shifts in the heavy–hole (hh) and light-hole (lh) band-edges, respectively, with reference to the conduction band, C_{11} and C_{12} are the elastic stiffness coefficients, b and d are the deformation potentials, and f is the strain, which is given by,

$$f = \frac{\Delta a}{a} = \frac{a-a_0}{a} \tag{2.3}$$

where, a and a_0 are the lattice constants of the layer and the substrate, respectively, and Δa is the lattice mismatch [7].

The schematic E-K diagram for an unstrained direct bandgap semiconductor is shown in figure 2.2 (a). The degeneracy in valence band at the Γ-point, observed in the case of unstrained QW, is lifted due to compressive and tensile strains as shown in figure 2.2 [b] and figure 2.2 [c], respectively. The biaxial compressive strain increases the splitting between hh and lh whereas the biaxial tensile strain decreases it. Change in splitting changes the interaction between the hh and lh bands, thereby changing the curvature of the bands and the correnspondingly hole-masses. Thus, strain also produces anisotropy in the valence band. The hh band becomes the lowest lying valence band in the case of compressive strain and the modified bandgap is given as $E_{g1} = E_g+\Delta E_{hh}$. Similarly, in the case of tensile strain, the bandgap gets modified as $E_{g2} = E_g+\Delta E_{lh}$ with the lh band becoming the lowest lying valence band.

The band structure modification, in the case of biaxial compressive strain, leads to the reduction in the valence band effective masses. The nonparabolicity of the subband structure due to the hh and lh band mixing is removed in consequence of the increase in the degeneracy between lh and hh. This results in improved matching between the density of states for the conduction band and the valence band due to the significant reduction in density of states in the valence band of a strained QW. Both these factors, due to the band structure modification, lead to the increase in differential gain, and consequently, lower the threshold current density for lasers with compressive strained QW as compared to the unstrained QW. In the case of tensile strain, the hh and lh states merge and the density of states in the valence band increases at low strain. For higher values of strain, the bands decouple again with the lh bands being higher in the energy, increasing the differential gain to reduce the threshold current. Thus both, compressive and tensile strain, results in improved characteristics of laser diodes.

Various techniques for the high quality epitaxial growth of high-power laser diodes based on III-V semiconductors are discussed briefly in the next section with focus on the MOVPE technique, which is employed for the growth of laser diode structure investigated in this thesis.

2.3 Epitaxial Growth Techniques

Several techniques are available for the epitaxial growth of III-V semiconductors and their heterostructures. These include liquid phase epitaxy (LPE), molecular beam epitaxy (MBE), and vapor phase epitaxy (VPE), etc.

2.3.1 Liquid Phase Epitaxy

Historically, the liquid phase epitaxy (LPE) technique played an important role in the early development of laser diodes. First AlGaAs/GaAs double heterostructure (DH) lasers operating at room-temperature were developed by the LPE [9,10]. Even the DH lasers with quantum size effects were also realized by LPE in the very beginning [11]. In LPE, an epitaxial layer is grown when a supersaturated solution is cooled systematically over a substrate in a clean environment, preferably ultra-pure hydrogen. Usually molten Ga or In are used to form the melt, and therefore LPE is commonly described as solution or melt growth. LPE is an equilibrium growth technique and the process of growth is governed by the laws of thermodynamic phase equilibria. The following equilibrium exists in the solution between atoms, A and C, and molecules, AC.

$$AC \leftrightarrow A + C \tag{2.4}$$

The equilibrium conditions depend very much on the temperature and on the concentration of the dissolved semiconductor in the melt. The growth of the layer from the liquid phase can be controlled by a forced cooling of the melt. Because of redistribution effect at the solution-solid interface, the impurity introduction can be strongly reduced in the epitaxial growth with this technique. The experimental setup for LPE is extremely simple and high quality layers can be grown.

In conclusion, it is fair to state that the LPE technique is characterized by simplicity of the equipment and the general safety associated with it. Expensive vacuum equipments are not required. Also, the deposition rates are high and the crystal quality is very good. Computer controlled equipment results in a high degree of reproducibility, and thickness and composition control. However, due to the nature of the growth from the melt, ultra-thin layers, less than 1000 Å, and hyper-abrupt junctions cannot be grown with precise control, making it less effective for the growth of laser diodes.

2.3.2 Molecular Beam Epitaxy

Molecular beam epitaxy (MBE) is conceptually a simple technique where directed thermal beams of atoms or molecules, which are evaporated from the heated effusion cells at a controlled rate, react on the substrate held at a high temperature under ultra-high-vacuum (UHV) conditions. The beam flux is controlled by effusion cell temperature. Abrupt junctions and doping profiles are realized by rapid switching of different beam species through mechanical shutters in front of the cells.

In MBE, the growth is carried out under non-equilibrium conditions and is principally governed by surface kinetic processes. The growth involves the adsorption of the constituent atoms or molecules, their dissociation and surface migration, and incorporation, to form the epitaxial layer. The cells are designed in such a way that realistic fluxes for crystal growth at the substrate can be realized, while the Knudsen effusion condition is maintained (i.e., the cell aperture is smaller than the mean free path of the vaporized effusing species within the cell).

The MBE allows high quality structure growth at relatively lower temperatures compared to the growth temperatures used for synthesis in MOVPE [12]. The in-situ growth monitoring techniques like reflection high energy electron diffraction (RHEED), low energy electron diffraction (LEED), or mass spectrometry, are suitable with MBE due to the UHV environment. AlGaAs Laser diodes emitting at 780 nm for CD players are grown in large quantities by MBE. This technique is also a leading contributor to the revolutionary progress in the device-physics caused by the occurrence of the new physical phenomenon using superlattice structures [13]. The limitations of the MBE lie in the operation and maintenance of the UHV equipments and to some extent, lower throughput for industrial applications. A major technical problem for MBE is the growth of phosphorus containing materials because of the high vapor pressure of phosphorus and the resulting difficulty with the pumping system [14].

To overcome the problems with phosphorus, a variant of MBE is developed in which, all the sources are either alkyl or hydride and the growth is carried out under UHV as in a usual MBE growth system. Further, a number of modified MBE techniques are also in practice. For example, in gas-source MBE (GSMBE) solid group III sources and

hydrides for group V are used. Metal-organic MBE (MOMBE) makes use of alkyl group III sources and elemental group V sources. Alkyl group III sources with hydride group V sources make chemical beam epitaxy (CBE). All these techniques integrate the advantages of MBE with various sources.

2.3.3 Vapor Phase Epitaxy

Vapor phase epitaxy (VPE), also called chemical vapor deposition (CVD), refers to the formation of a condensed phase from a gaseous medium of different chemical composition. VPE is different from the physical vapor deposition (PVD) process such as e-beam evaporation, sputtering or MBE, where condensation occurs in the absence of a chemical change. In VPE, a mixture of gases stream through a reactor and interact on a heated substrate to grow an epitaxial layer. There are three different CVD techniques used for the growth of III-V and other compound semiconductors. These are the halide process, hydride process, and the metal-organic vapor phase epitaxy (MOVPE).

2.3.3.1 Metal-Organic Vapor Phase Epitaxy

MOVPE or metal organic chemical vapor deposition (MOCVD) is an improvised form of VPE technique where the growth is carried out from the vapor phase using organometallic and hydride sources [8,15]. It was first developed extensively by Manasevit in 1968 for the growth of a variety of materials including III-V semiconductors [16]. Since then, it has been advancing as a significant technique for the growth of single layers, heterojunctions, and QW structures with excellent control over layer thickness, doping, and formation of hyper-abrupt isotype and anisotype junctions. It was the MOVPE technique, which led to the room-temperature operation of QW lasers for the first time [17] by means of the high quality epitaxial layer structures.

In MOVPE, metal-organic (MO) precursors, usually the alkyl compounds of group III elements, i.e. Al, Ga or In react with sources of group V element, As and P, usually the hydrides arsine (AsH_3) and phosphine (PH_3), on a heated substrate to form the epitaxial layer. Hydrogen is, normally, used as a carrier gas at atmospheric or reduced pressures. Laser diode structures are usually grown at low pressure, about 100 torr. The basic chemical reaction is irreversible pyrolysis that takes place in the vapor phase,

forming some intermediate compounds. Finally, the constituent elements are released and get incorporated into the lattice on the semiconductor surface. The substrate wafer is mounted on a rotating graphite holder or susceptor that is held at growth temperature by RF heating.

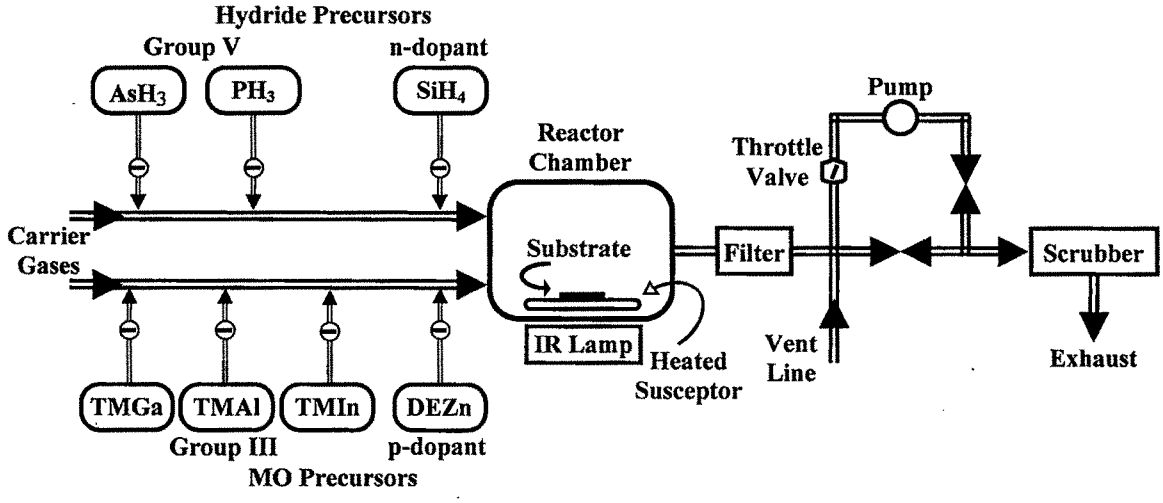

Figure 2.3: A typical MOVPE growth system.

A typical MOVPE growth system is shown in figure 2.3. It can be divided into three main parts; a gas-mixing system, the reactor, and the pump and exhaust handling system. In the gas-mixing system, the MO precursors are kept at a precisely-controlled temperature and pressure. These precursors are usually liquid (TMGa, TEGa, TMAl, DMZn) or solid (TMIn) and flowing the hydrogen through these precursors results in a controlled transport of their saturated vapor into the reactor. The reactants can be switched into the reactor or bypassed directly into the exhaust by switching manifolds [18].

The reactor design can either be horizontal linear reactor [19] or vertical reactor. Fabrication of the first MOVPE grown AlGaAs diode lasers was reported using vertical reactor [20]. However, horizontal reactors are now used extensively for the production of high-power laser diode structures.

The reactor chamber is followed by a pumping system consisting of a rotary pump, a throttle valve for pressure control, and traps for particles or condensable

materials. Wet or dry chemical scrubbers are used to remove the toxic materials from the effluent gas coming out of the reactor.

A number of important and beneficial features are offered by the MOVPE growth technique. Compounds, such as GaAs, can be grown with different As to Ga ratio (V/III ratio) simply by varying the relative vapor pressure of AsH_3 and trimethyl gallium (TMGa) as there is no need of establishing equilibrium with source materials. This allows the study of native defects and trap states, which are supposed to be related to the stoichiometry. It is possible to grow almost all the III-V semiconductor compounds, their ternary and quaternary alloys using MOVPE. Growth of high purity, ultra-thin layers and abrupt junctions with precise composition and doping control make this technique prevailing in the field of optoelectronic device fabrication.

The comparison of strengths and weaknesses of these epitaxial growth techniques are listed in table 2.1 [21].

Table 2.1: Comparison of strengths and weaknesses of various epitaxial growth techniques.

Technique	Strength	Weakness
LPE	Simple, high purity	Commercial production, inflexible, Non uniformity
MBE	High Uniformity, High purity GaAs, Abrupt interfaces, In-situ growth monitoring	As/P alloy difficult, 'Oval' defects, Low throughput, Need UHV conditions
MOVPE	Most flexible, High purity, Abrupt interfaces, Low interfacial recombination velocity, High Uniformity, Large scale, In-situ growth	Expensive reactants, More parameters to control accuracy, Hazardous precursors (especially using Hydrides)

2.4 Growth of III-V Semiconductors using MOVPE

2.4.1 Chemical Reactions and Precursors

In MOVPE growth process, the basic chemical reaction for the deposition of compound semiconductors and alloys involves a pyrolysis reaction of the vapors of a volatile metal-organic compound and a gaseous hydride, given by [15]

$$R_nA + DH_n \rightarrow AD + nRH \tag{2.5}$$

where, R_n indicates a lower order organic radical, such as a methyl- or ethyl-radical; A and D are, respectively, the group III and V constituent species for the deposited solid. An important example of this simplest case is given by

$$(CH_3)_3Ga + AsH_3 \rightarrow GaAs + 3CH_4 \tag{2.6}$$

The growth of ternary and quaternary semiconductor alloys can easily be realized by mixing the vapors of the different alloy constituents in the appropriate vapor phase ratio to form the required composition. A general equation for a ternary alloy is given by

$$xR_nA + (1-x)R_nB + DH_n \rightarrow A_xB_{(1-x)}D + nRH \tag{2.7}$$

For example, the reaction for ternary InGaP is given as,

$$x(CH_3)_3In + (1-x)(CH_3)_3Ga + PH_3 \rightarrow In_xGa_{(1-x)}P + 3CH_4 \tag{2.8}$$

For quaternary compounds, the general equation is given as,

$$xR_nA + (1-x)R_nB + yDH_n + (1-y)EH_n \rightarrow A_xB_{(1-x)}D_yE_{(1-y)} + nRH \tag{2.9}$$

Quite a few metal-organic compounds have been studied extensively as source precursors for the MOCVD growth process. An ideal precursor for MOVPE must have adequate vapor pressure near room-temperature to provide reasonable growth rates. It must allow sufficient purification. Also, controlled interaction with other species or materials in the growth ambient is very important. Intrinsic incorporation of unwanted impurities like carbon must be negligible. It must exhibit controlled decomposition at growth temperatures and high stability during storage. The most popular among various metal-organic compounds are trimethyl gallium (TMGa), trimethyl aluminum (TMAl), and trimethyl indium (TMIn).

Compound semiconductors comprise two or more elements with different vapor pressures. The evaporation rate of the anion element may be higher than that of the cation above the congruent sublimation temperature, T_c, which is, in general, lower than the growth temperature. This necessitates an excess supply of the volatile species during the growth to avoid material decomposition [22]. Thus, for the growth of III-V compounds, precursor of group V is delivered in excess continually and the deposition begins when the column III precursors are introduced into the reactor. The mole fraction of the column III elements generally determines the growth rate. Moreover, the decomposition of the column V hydrides (ASH_3 and PH_3) is much less efficient than that of the column III metal-organics at normal growth temperatures. This requires the ratio of mole fractions of column V to column III species (V/III) to be much greater than one during growth.

2.4.2 Growth Mechanism

For any growth process occuring in a regime of viscous flow, the hydrodynamics of the reactor geometry has a great influence on the nature of the process and the growth optimization is reactor-specific. Typical processes that take place in the reactor during growth are schematically shown in figure 2.4.

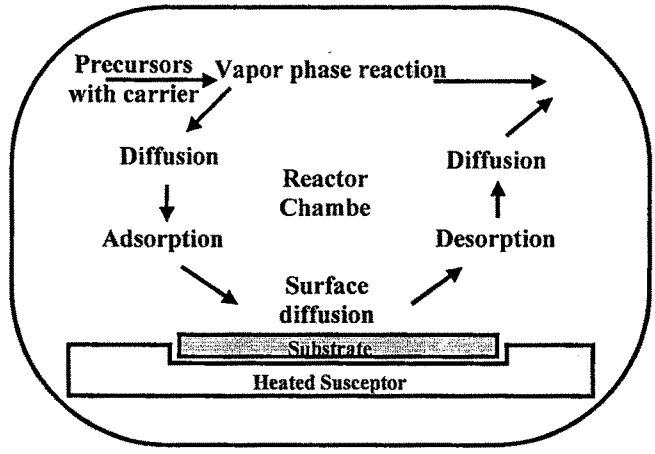

Figure 2.4: Processes in MOVPE reactor during the epitaxial growth.

Deposition takes place in the growth chamber, which is constructed of quartz. The substrate wafer is mounted on a graphite holder or susceptor that is held at growth temperature, usually by RF heating. Upon entering the reactor, the precursors mix and may initially decompose in the hot region above the substrate. Deposition occurs on hot surfaces which include the substrate, susceptor, and portions of the quartz reactor. The

susceptor is rotated in order to improve the deposition uniformity. Thus, growth proceeds through a series of steps as shown in figure 2.4: the precursors diffuse from the gas stream to the substrate region, precursor decomposition occurs near or on the substrate, the new material is incorporated into the growing layer through adsorption, surface diffusion, surface reactions, and finally, the reaction by-products are removed through diffusion.

2.4.3 Growth Regimes

As discussed in section 2.4.1, the MOVPE growth process is generally performed under conditions of nonstoichiometric, excess, and usually continuous column V species gas flows to compensate their lower pyrolysis efficiencies and much greater volatility of atoms in the desired solid films. Thus, flow of column III alkyl constituents decides the growth rate of MOVPE epitaxial layers. Three distinct growth regimes [23] can be observed subject to the growth temperature in MOVPE. The first regime is the reaction-rate limited growth, also called kinetically limited growth. This is dominant at relatively low temperatures, where pyrolysis efficiency is less and occupies a narrow temperature range. Above certain temperature where the pyrolysis efficiency reaches unity, the growth rate almost becomes independent of the temperature. This regime is called the mass-transport limited [24]. This regime is usually wide and exists in the range of a few hundred degrees Celsius. Most of the III-V semiconductor compounds are grown in this regime. The growth, in this regime, is governed by diffusion process instead of pyrolysis efficiency. However, the gas-phase diffusion coefficient of the alkyls is nearly independent of the temperature and so is the growth rate. At further higher temperatures, even the regions away from the substrate in the reactor becomes hot enough to trigger the gas-phase pyrolysis reaction forming solid particulates without being deposited on the substrate. This parasitic spontaneous nucleation [25] takes place at the cost of the layer deposition and reduces the growth rate.

2.4.4 Growth Rate

In the mass transport limited growth, as is the case for most of the III-V compounds, a simplified picture of the growth process can be described through a concentration boundary layer to the substrate as the rate-limiting step [26]. The boundary layer can be

considered as a gas-phase region, with little growth-rate-limiting constituent i.e., the column III precursor. The gas is homogeneous in the initial portion of the deposition zone. However, more and more material is depleted from the gas phase as it passes over the substrate to form the deposited layer. Therefore, the thickness of this boundary layer, δ_d, increases with distance along the gas flow direction, and can be expressed as [27]

$$\delta_d = 3\left(\frac{D}{v}\right)^{\frac{1}{3}}\left(\frac{vl}{V}\right)^{\frac{1}{2}} \tag{2.10}$$

where, D is the diffusion coefficient, v is the kinematic viscosity, l is the distance down the reactor, and V is the velocity of gas in the reactor. The flux to the substrate, which determines the growth rate, is then given by

$$F = -D\frac{dC}{dy}\bigg|_{surface} \approx -D\frac{C_0}{\delta_d} \tag{2.11}$$

where C_0 is the initial concentration of the rate-limiting species in the gas phase. It is evident from this expression that the growth rate is linearly proportional to the concentration of the rate-limiting species. However, this is an oversimplified model and the simple concept of a concentration and boundary layer is not sufficient for precise modeling of the growth rate, uniformity of deposition and doping in practical reactors.

There exist a number of factors complicating the growth mechanism in the fluid-thermal environment and must be taken into consideration while optimizing the growth process. One of them is the large thermal gradients between the hot susceptor and the cold walls of the reactor. Such thermal gradients can result in the formation of thermal convection cells within the reactor. These cells cause recirculation of partially reacted gases back into the input gas stream, increasing the effective residence time for the reactive ingredient or dopant species. Such recirculations lead to the degradation of the growth rate uniformity as well as the material-properties. The rapid switching of the reactants in the gas stream is also hindered by such recirculations, spoiling the formation of abrupt metallurgical and electronic junctions. Such thermally driven convection cells can be reduced significantly by reducing the reactor pressure [28].

In a nutshell, the MOVPE growth is quite a convolutionary process and provides a variety of growth approaches for a particular material system.

2.4.5 Doping of Semiconductors

The operation of a laser diode requires the presence of a p-n-junction. For usual applications the lower cladding, and sometimes also the lower waveguide layers, are grown n-type on an n-type substrate; and the upper cladding and upper waveguide layers are doped p-type. The location of the p-n-junction, the series resistance, especially in the p-type layers, and the losses due to free carrier absorption, depend on the doping-profile and the doping-level and are crucial in the case of high-power laser diodes. Thus, a good control of these features is necessary.

For controlled doping-profile, the dopant must be placed in the structure accurately, which is governed by the precursor used, its interaction, if any, with the growth system, and the vapor pressure of the element itself. Further, the subsequent movement, i.e. the redistribution of the dopant element, must be minimized in the crystal. This is controlled by diffusion of the element in the host material. Moreover, many of the dopant precursors exhibit the *memory effect*. This arises from the fact that some reactor parts, especially interior surfaces, absorb the dopant species initially after they are introduced in the chamber and do not allow efficient doping for some time until they get saturated by such dopant species. Similarly, when the dopant is turned off, the concentration of dopants in the reactor decreases slowly instead of abrupt fall due to desorbtion of dopant species from the interior surfaces of the reactor. Moreover, the dopant profile may change during subsequent growth if the solid-state diffusion coefficient of the dopant is large. Thus, the ideal dopant would have no memory effect and a low diffusion coefficient. The percentage of electrically active dopant to the metallurgical concentration of the dopant should be high, ideally unity. Ideal dopant sources have a linear or sublinear dependence on the mole fraction of the precursor in the gas phase, and are not sensitive to other growth conditions such as temperature, pressure, or V/III ratio.

2.4.5.1 Donors

A large number of elements have been used as donors in III-V materials, including Si, Sn, and Ge from group IV, and S, Se, and Te from group VI of the periodic table. Si, Sn, and Ge, though amphoteric, are all incorporated as donors in the MOVPE technique.

Although Sn, Se, S, Ge, and Te can be incorporated as donors in MOVPE through their appropriate precursors, the incorporation of these dopant-elements decreases with increasing growth temperature or V/III ratio. In addition, they are characterized by a fairly strong memory effect, which makes production of abrupt dopant junctions difficult.

The donor which most closely approaches the ideal criteria listed above is Si, using precursors like Si_2H_6 or SiH_4. Si incorporation from Si_2H_6 is independent of growth temperature for pressures 60 torr [29], whereas Si incorporation from SiH_4 is kinetically limited, as evidenced by the dependence on growth temperature and substrate orientation. This is because pyrolysis is quite slow due to homogeneous SiH_4 at typical growth temperatures. Both of these precursors exhibit little memory effect, and the diffusion coefficient of Si in GaAs is quite low, making it ideal for use in structures which require abrupt donor profiles.

2.4.5.2 Acceptors

The elements Be, C, Cd, Mg, and Zn have all been used as acceptor dopants in MOVPE. Among them, C, Mg, and Zn are the most commonly used p-type dopants. The incorporation of Zn, Mg, and Cd shows some temperature dependence and are characterized by a memory effect. Carbon is the dominant unintentional acceptor in GaAs and $Al_xGa_{1-x}As$. However, it is also used as an intentional dopant [30]. Carbon incorporation, too, shows strong temperature dependence. However, there are two major advantages of carbon over zinc: the absence of a memory effect, and a lower diffusion coefficient. Nevertheless, zinc, with its precursors dimethyl zinc (DMZn) and diethyl zinc (DEZn), still dominates as p-type dopant in MOVPE growth of laser diodes.

2.5 Characterization Techniques

The MOVPE grown layers were characterized by various techniques like high-resolution x-ray diffractometry (HRXRD) [31], photoluminescence (PL), and electrochemical capacitance-voltage (ECV) profiling. These techniques are briefly discussed below.

2.5.1 High-Resolution X-Ray Diffractometry

High-resolution x-ray diffractometry (HRXRD) is a powerful tool for structural characterization of grown epilayers and bulk material. The structural properties of the material are the basis for the physical properties including electronic and optical properties. Most III-V Semiconductor materials, for example, GaAs, GaP, InAs and InP binary materials and their various alloys have the space group of $F\bar{4}3m$, commonly known as the zincblende structure. This structure can be visualized as two interpenetrating face-centred cubic (FCC) lattices displaced along the body diagonal by one fourth of the lattice constant. With HRXRD, quick and non-destructive characterization is possible for the basic epitaxial layer parameters like layer composition, strain, lattice-mismatch, and thickness.

The principle of x-ray diffractometry technique is based on elastic scattering of x-ray from periodically arranged atoms or complex groups of atoms that form sets of lattice planes in a crystal. Different planes in a crystal have different interplanar spacing d, which is a property of the material. Diffraction takes place when the condition for constructive interference is satisfied i.e., when the path difference between the scattered rays from successive planes is an integral multiple of the wavelength λ. This is expressed by the Braggs law as,

$$n\lambda = 2d\sin\theta \tag{2.12}$$

where, θ, the Bragg angle, is the angle between the incident x-ray beam and the lattice planes.

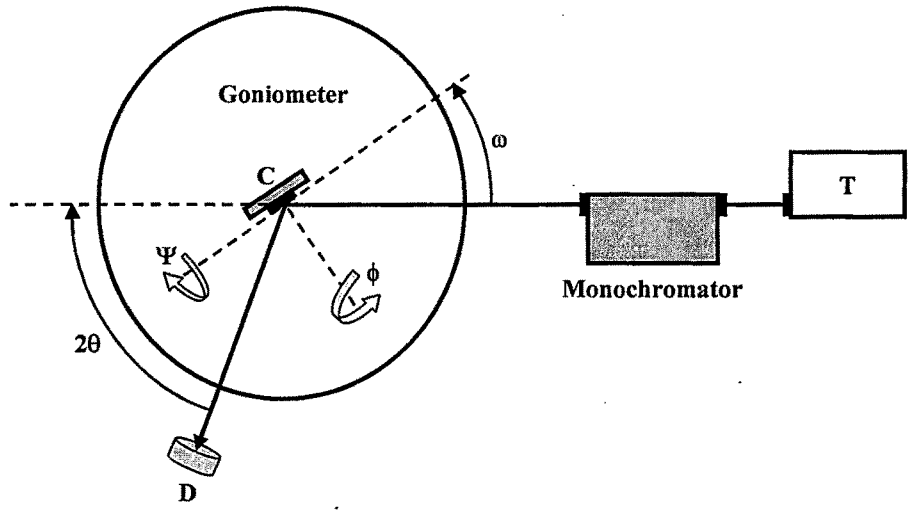

Figure 2.5: Schematic diagram of experimental set up for HRXRD.

Essential features of the x-ray diffractometry set up are shown in figure 2.5. X-rays from the tube T ($CuK\alpha_1$ - 1.5406 Å) are incident on the crystal C, which may be positioned at a desired angle θ with respect to the incident beam. D is a detector which measures intensity of the diffracted x-rays and can be positioned at any desired angle [32]. The incident beam, normal to the reflecting plane and diffracted beam are always coplanar. The angle between the diffracted beam and transmitted beam is always 2θ, which is known as diffraction angle. In the ω scan (rocking curve scan) method, value of 2θ (i.e. position of detector) is kept fixed and ω is varied. While in ω/2θ scan method both ω and 2θ are varied. ω/2θ scan is usually performed on the (004) reflection of the sample.

The lattice parameter and the mismatch can be determined precisely with the help of HRXRD, and the chemical composition of the compound can be deduced from these data. When x-rays are incident on the sample, they get diffracted from different layers having different composition i.e. different lattice constants at different angles. It means that for different composition the diffraction angle gets changed. The detector measures the intensity corresponding to diffraction angles, which reveals the information regarding the lattice constants of the materials in the compounds. For any plane (h, k, l) in a cubic system with lattice constant a, the inter-planar spacing d is given as,

$$d = \frac{a}{\sqrt{\left(h^2 + k^2 + l^2\right)}} \tag{2.13}$$

To determine the lattice mismatch, we use differentiated Bragg's equation as,

$$\frac{\Delta d}{d} = -\Delta\theta \cot\theta \tag{2.14}$$

where, Δd/d is the lattice-mismatch between the layer and the substrate, Δθ is the angle-difference between substrate and layer reflections, d is the spacing for a particular reflection and θ is the Bragg angle.

With the help of Δd one can find out the value of lattice constant of an epitaxial layer. The lattice parameters of alloys gradually change with the alloy composition and can be approximated by a linear interpolation of the lattice parameters of the binary end

members. This is known as Vegard's law. The composition 'x' in an alloy is calculated from the relation,

$$a_{A_xB_{1-x}C} = xa_{AC} + (1-x)a_{BC} \tag{2.15}$$

where, AC and BC are binary compounds such as InP, GaP.

The intensity of scattered x-rays depends on the scattering volume, i.e. the thickness of the layer. So, a rough estimate of the thickness can be obtained from the intensity. However, if the sample contains layers with very smooth interfaces, they give rise to fringes which are observed in the form of a high frequency modulation of the layer signal. This allows a precise measurement of the layer thickness.

For the determination of chemical composition with an accuracy of 1%, the reflection must be accurate by $\Delta\Omega = 0.001^0$. Thickness of the epitaxial layer can also be calculated from HRXRD. To resolve thickness fringes of 2 μm thick layer, resolution of $\Delta\Omega = 0.0026^0$ is required in the measurement of angle-difference. HRXRD in combination with PL or SPS can give the chemical composition for quaternary layers. In order to determine the chemical composition for a quaternary alloy, two composition-dependent material parameters are required, viz., the lattice constant using HRXRD, and the bandgap using PL or surface photovoltage spectroscopy (SPS) independently. The x-ray diffractometry techniques are making it possible to correlate the structural properties of the epitaxial growth processes, to the electrical and optical properties and to the device performance.

2.5.2 Photoluminescence Spectroscopy

Photoluminescence (PL) spectroscopy has enormous potential to examine and characterize materials and the dynamical processes occurring in materials. This technique is based on the optical excitation of the sample and the measurement of energy distribution of the emitted photons. This energy distribution unveils the information regarding properties of the material like bandgap, free carriers, impurity, defects including defect-species and defect-concentrations, and possible stimulated emission, etc [33]. The sample is excited with the help of an intense beam, usually a laser, of photon energy greater than the bandgap of the semiconductor sample, which results in generation

of electrons and holes in the sample. These electrons and holes quickly recombine, with various possibilities as shown in figure 2.6, to emit the radiation with different energies. E_C, E_V, E_d and E_a show the relative positions of the conduction band, valence band, donor level, and the acceptor level, respectively, in figure 2.6. An electron, excited by the pump-beam from the valence band to the conduction band (process 1), first relaxes to the bottom of the conduction band by emission of phonons (process 2). Then it may get de-excited by combination of various downward electron transitions, like, band to acceptor level (process 3), band to donor level (process 4) donor level to acceptor level (process 5), acceptor level to band (process 6), and band to band (process 7). Depending on the measurement conditions and the sample to be investigated, it is possible to observe a PL corresponding to any of the above-mentioned mechanisms.

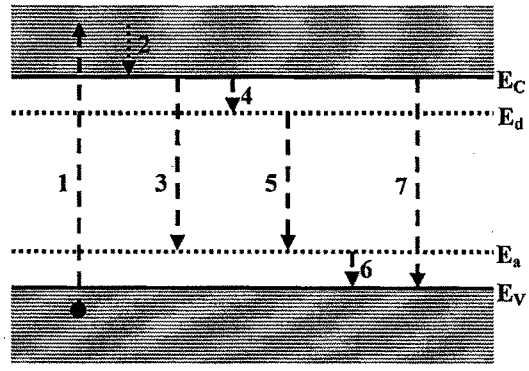

Figure 2.6: Various possible transitions in the PL spectroscopy.

This technique for material characterization has achieved significant success, at least partly due to the simplicity of the technique and the absence of sample-processing requirements.

A typical PL measurement system consists of an excitation source, a variable temperature cryostat, sample holder assembly, a photo detector and a lock-in amplifier. The experimental set up is shown in figure 2.7. In the figure, S, L, F, C, MC, and PMT, indicate the sample, lenses, high-pass filter, chopper, monochromator, and photomultiplier tube, respectively. Lasers are mainly used as the excitation source due to their high intensity and directionality. According to the bandgap of the material, lasers emitting at different wavelengths like He-Cd laser (325nm), second harmonic diode pumped Nd:YAG laser (532 nm), laser diode (808 nm) etc., can be used. The laser beam is incident at an angle on the sample and focused with the help of a convex lens. A

mechanical chopper is used to chop the the laser beam. The PL, emitted by the sample is focussed by the assembly of lenses on the monochromator slit. The PL signal is measured by detector (photomultiplier tube), and fed to the lock-in amplifier.

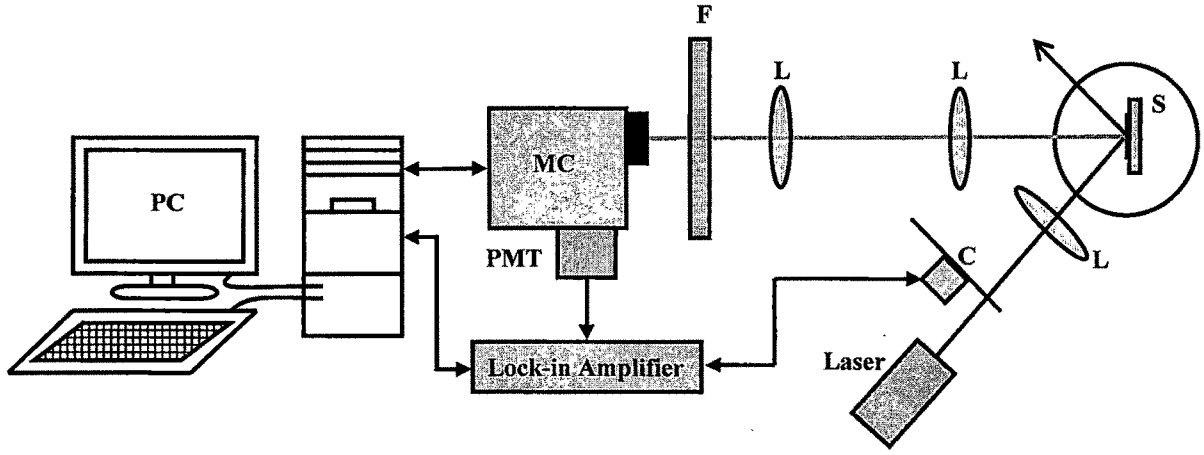

Figure 2.7: Schematic diagram of the experimental set up for PL spectroscopy.

Since, PL provides a direct measure of the optical quality of the samples for epitaxial layers, it is very useful for the characterization of materials, especially for optoelectronic devices like LEDs and laser diodes. The measurement technique is very simple, non-destructive, and requires little or no sample preparation. Its main limitation is a weak or no PL signal for indirect bandgap materials. It provides only the lowest excited state information for quantum structures and requires low temperatures to suppress the luminescence from defects in case of low quality samples.

2.5.3 Electrochemical Capacitance Voltage Profiling

For fabrication of laser diode, it is necessary to know the carrier concentration of different layers of the multilayer structure at different depths for optimum device-properties. This can be achieved by capacitance-voltage (C-V) measurements. Studies of capacitance associated with the depletion region of a Schottky barrier or an abrupt p-n junction provide extensive information about the concentration and characteristics of electrically active centers in the epitaxial layers.

In CV profiling method, the capacitive component of the impedance of the depletion region of Schottky barrier or p-n junction is measured at different bias voltages

to obtain a capacitance-voltage curve. Under "depletion approximation", capacitance of a depletion region is given by [34],

$$\frac{1}{C_j^{\,2}} = \frac{2(V_b - V_a)}{A^2 e\varepsilon N_d} \tag{2.16}$$

where, C_j is a junction capacitance, N_d is doping density, V_b is built-in voltage, V_a is applied bias, and A denotes the area. Thus, a plot of inverse C_j^2 versus V_a i.e., the applied reverse-bias voltage, gives a straight line. The doping density can be obtained from the slope as,

$$slope = \frac{2}{A^2 e N_d \varepsilon} \tag{2.17}$$

$$\therefore N_d = \frac{2}{A^2 slope * e\varepsilon} \tag{2.18}$$

The built-in voltage, V_b can be found from the intercept of the plot. However, the maximum depth which can be profiled by the conventional C-V profiling is restricted by electrical breakdown to a distance corresponding to the total space charge of about $2x10^{12}$ per cm^2. This limitation is often overcome by repeated chemical etching using electrochemical capacitance-voltage (ECV) profiling.

The ECV Profiling involves electrochemical etching followed by C-V measurements, which can provide the information about carrier doping concentration, type of dopant, structure imperfections, and thickness of the layer, etc. Figure 2.8 shows schematic diagram of a typical cell used in the electrochemical C-V Profiler. The semiconductor slice is held against a sealing ring, which defines a contact area. The etching and measuring conditions are controlled by the potential across the cell and this is established by passing a DC current between a semiconductor and the carbon electrode to maintain the required overpotential measured potentiometrically with reference to the saturated calomel electrode (SCE). In n-type material the reaction is promoted by holes, which are generated optically by illumination with blue light, which is strongly absorbed in the near surface region of the semiconductor. In the p-type material dissolution is affected by the flow of holes which occurs with the barrier under forward bias. The AC

signals are measured with respect to a Pt electrode located near the semiconductor surface to reduce the series resistance due to the electrolyte [35].

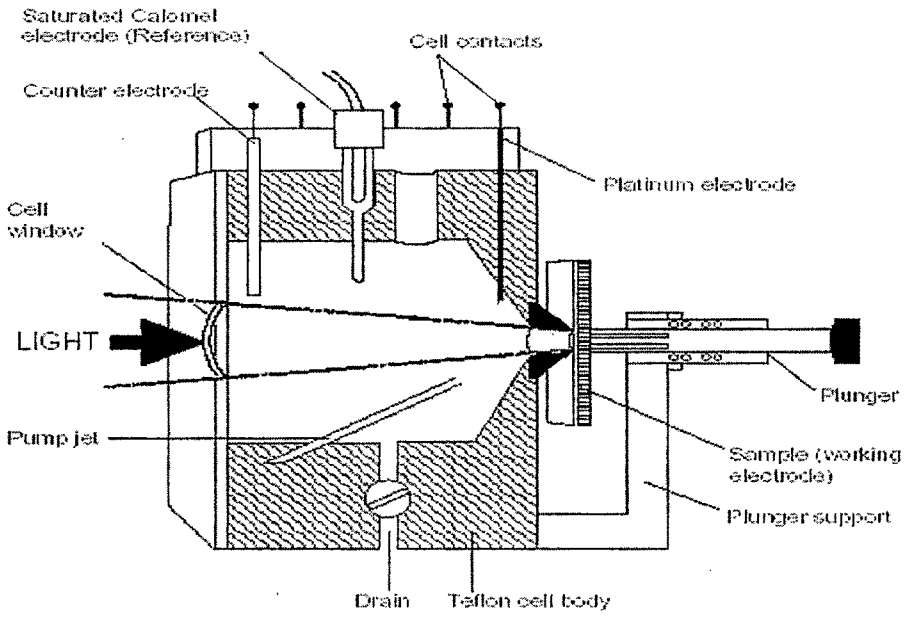

Figure 2.8: Schematic diagram of electrochemical cell.

The key to successful profiling is the choice of electrolyte. The electrolyte must have following properties;

- The electrolyte must be transparent to the illumination used for etching.
- It should be non corrosive with low series resistance [35].

The main advantage of ECV profiling is its ability to directly measure the electrically active carrier concentration, in contrast to the conventional metrology methods, such as SIMS, which detect only the chemical concentration of the dopant species. The key performance parameters such as forward voltage and contact resistance of the device are determined by electrically-active carrier concentration.

2.6 Growth and Optimization of Laser Structure

We optimized the MOVPE growth conditions for InGaP QW laser diode emtting in the red portion of the visible spectrum at the wavelength of around 670 nm. Laser diodes emitting in the range of 630 nm to 670 nm have found tremendous applications. The red laser diode is seen as a next substitute for the conventional He-Ne gas laser in many applications like

bar-code scanning, optical experiments, ranging, maping, spectroscopy etc. They are also used in optical recording in the interior of Digital Video Disc (DVD) and laser printers [36]. Red diode arrays are used as pump source for various tunable, Chromium doped, solid state laser materials such as alexandrite, $LiSrAlF_6$ and $LiCaAlF_6$ [37].

A typical laser diode structure consists of an active-layer QW sandwiched between two thin layers made up of the material with wider bandgap than active layer and consequently lower refractive index forming waveguide. Active region confines the injected charge carriers effectively into the well and to force them to recombine radiatively. In both sides of the waveguide layers, much thicker claddings, made up of further wider bandgap materials are grown. Cladding layers are doped with appropriate dopants to make p- and n-type layers, to constitute the p-n diode. On the upper cladding layer, a thin cap layer is grown which provides a platform to create further insulation and metallization. The structure is grown on a suitable substrate with a buffer layer.

2.6.1 Materials for High-Power Laser Diodes

Energy bandgap and lattice constant of the material are the key parameters in the material selection for laser diodes. The elemental semiconductors e.g. Si, Ge are not used for lasers because of their indirect bandgap. On the other hand, the compound semiconductor materials offer the required properties for the development of laser diodes. III-V semiconductor compounds are widely used for the fabrication of high-power laser diodes. The III-V binary compounds are formed by combining elements from group III and group V of the periodic table. Further, binary compounds can be combined or alloyed to form ternary or quaternary compounds. The bandgap as well as lattice constant of ternary and quaternary compounds are dependent on the mole fraction of the binaries, which are used for their formation. As the alloy composition changes, the band structure, and hence electronic and optical properties of the alloy change. Thus by choosing appropriate compounds or alloys, it is possible to select and tune the bandgaps and consequently the emission wavelengths for laser diodes.

Laser diode often faces rapid degradation in its performance due to formation of misfit dislocations in the crystal. To avoid this problem, thick waveguide and cladding layers have to be grown lattice matched to the substrate. The density of point defects, which

act as centers for non-radiative recombination to reduce the efficiency, shoud be as low as possible. Moreover, the crystalline quality of the layers can be adversely affected by ordering as in the case of GaInP or by phase separation as observed for certain compositions of quaternary GaInAsP [38]. These require optimal growth conditions for each material.

The choice of material system for the fabrication of laser diode is driven by the wavelength of interest. The emission wavelength of laser diode depends on bandgap of the active region in the laser structure as,

$$E_g = \frac{hc}{\lambda} \tag{2.19}$$

$$\text{i.e., } E_g(eV) = \frac{1239}{\lambda(nm)} \tag{2.20}$$

Hence, for red lasers with the emission wavelength in the range of 630 nm to 670nm, the bandgap of the material used in the active region must be within the range of 1.85 eV to 1.96 eV. The energy bandgap and lattice constant (equilibrium interatomic spacing) for various semiconductors at 0 K [39] is shown in figure 2.9. This plot suggests that the suitable materials for red lasers with the wavelength range of our interest are AlGaAs and InGaP alloys.

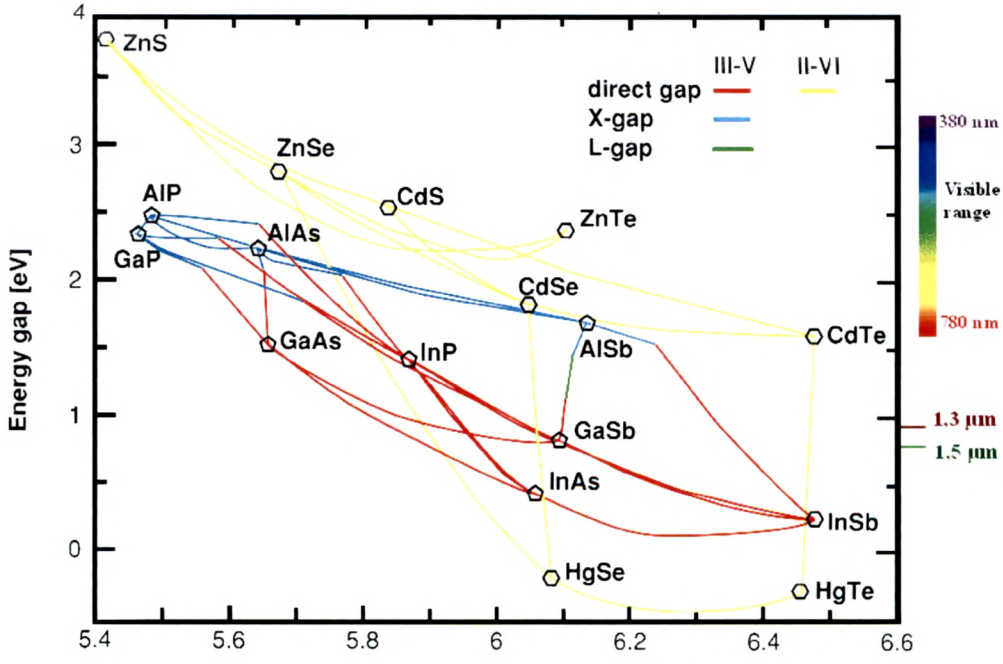

Figure 2.9: Bandgap versus lattice constant for conventional III-V semiconductors at 0K.

Some physical parameters of these ternary semiconductor compounds are interpolated by the parameters of their constituent binaries. For example, lattice constant of any ternary compound ($A_xB_{1-x}C$) is calculated with the help of Vegard's law [6] using equation (2.15). Similarly, the energy bandgap of any ternary compound ($A_xB_{1-x}C$) can be calculated as,

$$Eg_{A_xB_{1-x}C} = xEg_{AC} + (1-x)Eg_{BC} + x(1-x)C_1 \qquad (2.21)$$

where, C_1 is the Bowing parameter of ternary material [40].

Some possible material systems for the fabrication of red laser diodes are briefly discussed below.

2.6.1.1 The InGaP/InAlGaP Material System

This system was first discussed by Casey and Panish long back in 1978 [41]. The ternary $In_xGa_{1-x}P$ system has a direct bandgap over most of its composition range. The crossover with the X-minima lies at about X = 0.7. The compositional dependence of the energy bandgap of $In_xGa_{1-x}P$ at room-temperature is given by [40],

$$Eg_{In_xGa_{1-x}P} = xEg_{InP} + (1-x)Eg_{GaP} + x(1-x)C \qquad (2.22)$$

where, C is the bowing parameter which is 0.65 for InGaP. The lattice constants of GaP and InP differ significantly, as can be seen from the figure 2.9 and Table 2.2 [36]. At X = 0.48, the material is lattice matched to GaAs substrate.

Table 2.2: Bandgap and lattice constant of constituent binary materials of the InAlGaP quaternary semiconductor.

Material	Direct Bandgap (eV)		Lattice constant(Å) 300K
	0K	300K	
InP	1.42	1.34	5.8697
AlP	3.63	3.56	5.4672
GaP	2.88	2.78	5.4505
GaAs	1.51	1.42	5.6532

If a Ga atom is replaced by an Al atom, there is hardly any change in the lattice constant of the material. Hence, in $In_xGa_{1-x}P$, keeping In content fixed at 0.48, we may partially substitute Al for Ga to vary the bandgap while maintaining a value of lattice constant more or less matched with the GaAs substrate. If we denote the fraction of Ga replaced by Al by 'y', then the quaternary system has the composition $In_{0.48}(Ga_{1-y}Al_y)_{0.52}P$. This alloy has a direct bandgap for values of 'y', i.e., Al fraction, up to about 0.65, where the crossover with X- minima occurs [36]. Further, $In_xAl_{1-x}P$ with x = 0.47 is also lattice matched to the GaAs and can be used as a cladding layer. Table 2.3 shows Bandgap and lattice constant of important lattice matched compositions of InGaP/InAlGaP/InAlP/GaAs material systems at room-temperature (300K).

Table 2.3: Bandgap and lattice constant of InGaP/InAlGaP/GaAs material system.

Material	Bandgap (eV) (300 K)	Lattice constant (Å)
$In_{0.49}Ga_{0.51}P$	1.895	5.6530
$In_{0.48}(Ga_{0.40}Al_{0.60})_{0.52}P$	2.226	5.6569
$In_{0.47}Al_{0.53}P$	2.397	5.6549
GaAs	1.420	5.6532

InAlGaP has a cubic zincblende structure similar to its constituent binaries. An important property of InGaP and AlGaInP materials is the presence of strong tendency to order the In atoms with Ga and Al atoms on the alternate planes resulting in CuPt like ordered structures [38]. The ordering has important influences on the electro–optical properties of material. The bandgap of ordered phase can be lower as compared to that of disordered phase by about 90 meV. The degree of ordering depends on the epitaxial growth conditions and the substrate orientation [36] and must be taken into consideration while optimizing the growth.

GaInP offers higher stability of the laser diode facets against catastrophic optical mirror damage (COMD) [42] owing to its lower surface recombination velocity and a much lower tendency for oxidation in comparision to AlGaAs. Thus, InGaP/InAlGaP/InAlP is a suitable system for red laser diodes

2.6.1.2 The ZnCdSe Material System

II-VI binary materials like ZnSe and ZnS and ternary ZnSSe material have also found application for visible lasers mainly in the blue region. Table 2.4 shows the bandgap and lattice constants for binary constituents of this material system at room-temperature. Though the ternary compound ZnSSe has a direct bandgap over the whole composition range, the lattice constant varies considerably (by about 4%) with the S content as can be seen from the Table 2.4 [36]. For lower content of S, the zincblende structure is more stable. The lattice constant of ZnSe is about 0.27% greater than that of GaAs allowing the growth on GaAs substrate.

Table 2.4: Bandgap and lattice constant of constituent binary materials of ZnCdSe material system.

Material	Direct Bandgap (eV) (300 K)	Lattice constant (Å)
ZnS	3.77	5.409
ZnSe	2.77	5.669
CdSe	1.70	6.04
GaAs	1.42	5.6532

In case of ternary compound ZnSSe, an exact match of lattice constant with GaAs is achieved at S content of 6%. Corresponding energy bandgap for this ternary composition is about 2.82 eV. Therefore, the difference of energy bandgap between ZnSe and ZnSSe lattice matched to GaAs is only 50 meV. Hence, ZnSSe/ZnSe is not a good candidate for hetrojunction system. Due to inefficient carrier confinement, a very high leakage current is expected from such a structure. To overcome the problem of thermal escape of charge carriers, another active layer i.e. ZnCdSe is sometimes used and ZnSe acts as an intermediate layer.

2.6.1.3 The AlInGaN Material System

Basic binaries of III-V nitride system, GaN and AlN are direct bandgap semiconductors with large bandgaps of 3.4 eV and 6.2 eV respectively. Table 2.5 shows bandgap and lattice constant of constituent binary materials of AlInGaN quaternary semiconductor. The incorporation of Al into GaN alters the lattice constant appreciably as shown in Table 2.5 [36].

Table 2.5: Bandgap and lattice constant of constituent binary materials of AlInGaN material system.

Material	Direct Bandgap (eV) (300 K)	Lattice constant (Å)
GaN	3.39	3.189
AlN	6.2	3.112
InN	1.9 / 0.7 [43]	3.548
GaAs	1.42	5.6532

InGaN is used to reduce the bandgap in order to shift the emission wavelength into the visible region. Thus, the AlGaInN system covers the wavelength span from 210 nm to 630 nm. The lattice constant of the material increases with incorporation of Indium content in InGaN. Thermal conductivities of the nitrides are relatively high compared to GaAs [36], which is a favorable property for the CW operation of laser diodes. However, it is not easy to obtain red laser from InGaN as the requirement of In content in InGaN is large and normally difficult to grow by MOVPE technique.

After considering the above points and the availability of resources, we set our choice of the material system on the conventional InAlGaP/InGaP lattice matched to GaAs substrate for the growth of red laser diode using MOVPE.

2.6.2 Experimental

The samples discussed here were grown by low pressure MOVPE technique in horizontal reactor MOVPE system (AIX 200) in class 1000 clean-room. The samples were grown at the reactor pressure of 50 mbar on GaAs (001) substrate using TMGa, TMAl, TMIn, AsH_3, and PH_3 as precursors. Silane (SiH_4) and diethyl zinc (DEZn) were used as n-type and p-type dopant sources, respectively. The growth temperature was varied from 670 °C to 770 °C for different layers. X-ray diffraction measurements were performed using a HRXRD (PANalytical X'Pert MRD Pro) equipped with a Ge (220) monochromator with an open detector in the scattering plane for $CuK\alpha_1$ x-rays (1.5406Å). The PL is performed using ¼ m Sciencetech monochromator with 2 nm band pass. The samples for PL were excited by the diode pumped second harmonic Nd:YAG laser operating at 532 nm and is detected by photomultiplier tube (PMT) and measured using lock-in amplifier (Eg & G 7260). For low-temperature PL from 10 K to 300 K, the setup is equipped with liquid-

hellium cryostate (ARS CCR) with temp controller. The electrochemical capacitance-voltage (ECV) profiling was carried out using a Bio-Rad PN4300 instrument equipped with a conventional three electrodes electrochemical cell using EDTA as an etchant [44]. The growth and characterization of epitaxial layers for laser diode structure were carried out at Semiconductor Laser Section, SSLD, RRCAT, Indore.

2.6.3 Optimization of Different Layers

Figure 2.10 shows the schematic of laser structure planned for the red laser diode. In order to get optimum device characteristics, the individual layer parameters have to be optimized. In this section we present results related to the optimization of individual layer growth.

p^+ GaAs cap layer
InGaP
p-InAlP cladding layer
InAlGaP waveguide layer
InGaP (QW)
InAlGaP waveguide layer
n-InAlP cladding layer
n^+- GaAs buffer
n^+- GaAs substrate

Figure 2.10: Schematic structure for red laser diodes.

2.6.3.1 InAlP Cladding layer

❖ Growth temperature

First we optimize the growth temperature for InAlP cladding layer on GaAs substrate using HRXRD technique. Two different samples 2107034 and 2107035 were grown at the growth temperatures of 680 °C and 770 °C respectively keeping the Indium input flux fixed. Figure 2.11 shows experimental $\omega/2\theta$ diffraction patterns for the (004) symmetric reflection for InAlP/GaAs samples at room-temperature.

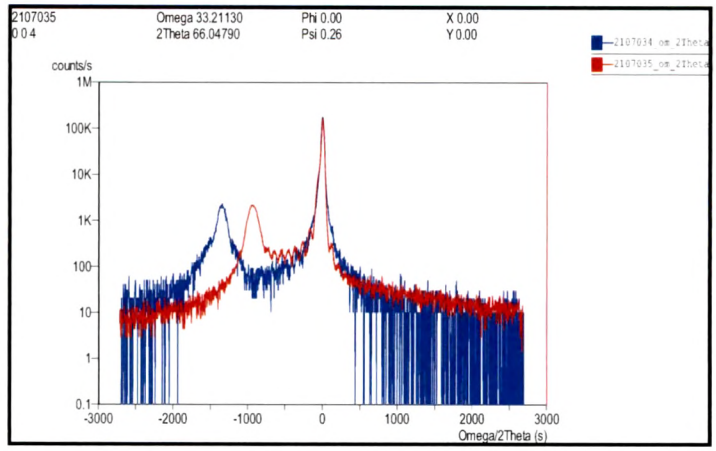

Figure 2.11: HRXRD pattern for samples 2107034 and 2107035.

Both curves show two peaks. More intense and sharp peak at the center corresponds to GaAs substrate. Another peak which is on the lower side of the substrate peak corresponds to the InAlP epitaxial layer. Small interference fringes observed between the InAlP layer peak and substrate peak are due to the interference of X-rays reflected from the top surface of InAlP and the interface between InAlP and GaAs. The composition of Indium in the two samples has been obtained by matching the experimental diffraction profile with simulated diffraction profiles obtained using X'Pert Epitaxy software. Table 2.6 shows results of Indium composition and lattice mismatch for both samples. The effect of growth temperature on the Indium incorporation and lattice mismatch is clearly observed.

Table 2.6: HRXRD results for samples 2107034 and 2107035.

Sample	**Material**	**Tg (^{0}C)**	**In (x_v)**	**In (x_s)**	Mismatch ($\frac{\Delta a}{a}$) ppm
2107034	InAlP/GaAs	680	0.6726	0.544	4916
2107035	InAlP/GaAs	770	0.6726	0.523	3390

Observation of nice interference fringes in sample grown at 770 °C indicates the better crystalline quality of the sample. The lattice mismatch observed is also lower for sample grown at 770 °C compared to the sample grown at 680 °C. Thus, we chose to grow InAlP at 770 °C.

❖ Lattice mismatch (Δa/a)

In order to get minimum lattice mismatch between InAlP and GaAs substrate, we have grown three samples of InAlP on GaAs substrate at 770 °C with different Indium flux to vary the In composition. The composition and lattice mismatch results obtained for these samples from HRXRD are given in Table 2.7.

Table 2.7: HRXRD results for samples grown by varying Indium composition.

Sample	Material	In (x_v)	In (x_s)	Mismatch (Δa/a) ppm
2107039	InAlP/GaAs	0.6133	0.4585	-1296
2107040	InAlP/GaAs	0.6296	0.4710	-388
2107047	InAlP/GaAs	0.6337	0.4720	-315

Large lattice mismatch (Δa/a), as is observed in sample 2107039 is not preferable for laser diode. The increased Indium composition in the ternary compound results in better lattice matching, in the case of sample 2107039 and 2107040, as shown in table 2.7. Thus, we decided to use conditions of sample 2107047 for the growth of InAlP cladding layer which shows 47.2% Indium composition in solid phase and the minimum value of mismatch (Δa/a). Figure 2.12 shows ω/2θ diffraction pattern for the (004) reflection for InAlP/GaAs sample optimized for minimum (Δa/a) at room-temperature.

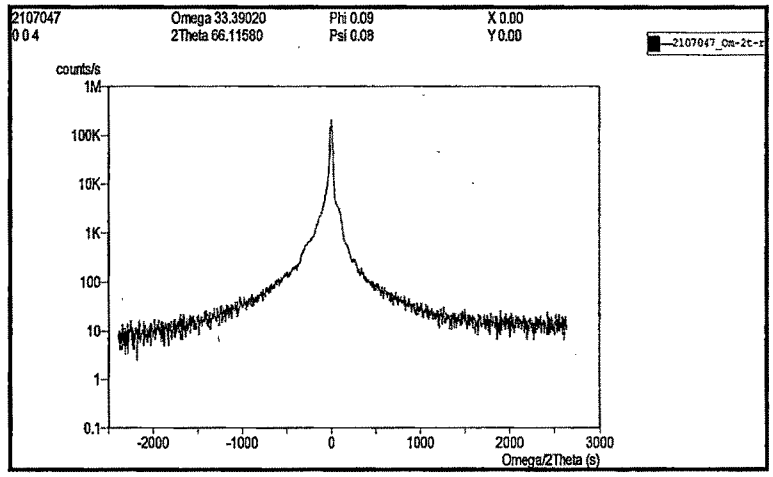

Figure 2.12: HRXRD pattern for sample 2107047.

❖ **n-type and p-type doping**

It is necessary to know the doping-density profiles of InAlP epitaxial layers in order to make good p-n junction. For optimization of n-type doping, three samples of InAlP layer on n^+-GaAs substrate with different flow-rates of the n-type dopant, SiH_4, were grown. The carrier concentration in these layers was obtained by ECV profiling. The doping concentration values measured from ECV Profiles are given in Table 2.8. We get sufficient doping concentration even at lower dopant to group III precursor ratio, i.e. 0.002. Even on increasing this ratio to 0.04, the increment in the doping concentration is not very large, as can be seen from the table. Thus, we choose the doping conditions of sample 2107053 for our laser structure.

Table 2.8: ECV results for n-type doping.

Sample	Tg °C	Dopant	Dopant/III %	Doping concentration
2107047	770	SiH_4	4	$3x10^{18}$
2107053	770	SiH_4	0.2	$1x10^{18}$
2107061	770	-	Undoped	$7x10^{16}$

Similarly, for the optimization of p-type doping, two samples of InAlP layer on n^+-GaAs substrate were grown with different flow rates of the p-type dopant, diethyl zinc (DEZn). The p-type doping values obtained from measured ECV Profiles are given in Table 2.9. However, we did not get notable difference in doping concentration by varying dopant to group III precursor ratio from 0.26 to 0.30. Hence, doping conditions of sample 2107081 were taken for the p-type doping in our laser structure.

Table 2.9: ECV results for p-type doping.

Sample	Tg °C	Dopant	Dopant/III %	Doping concentration
2107081	700	DEZn	26	$3x10^{17}$
2107082	700	DEZn	30	$3x10^{17}$

2.6.3.2 InAlGaP Waveguide layer

In the next step, we optimize InAlGaP quaternary waveguide layer for the red laser diode. The lattice matched InGaAlP on GaAs is optimized by varying constituent composition at

fixed growth temperature 770 °C. Three InGaAlP on GaAs samples were grown with different Indium flux X_V, i.e., 0.5921, 0.5839 and 0.5882. Figure 2.13 shows HRXRD results for these three samples of InGaAlP quaternary material grown on GaAs.

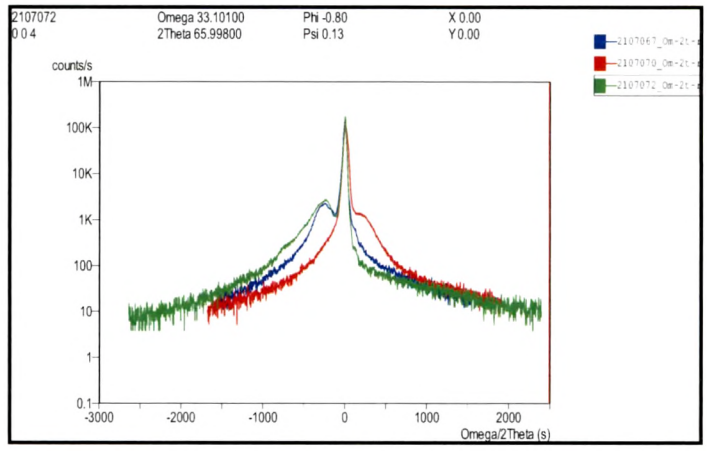

Figure 2.13: HRXRD pattern for samples grown by varying constituent compositin of InGaAlP.

Table 2.10 shows HRXRD results for these samples with different compositions. As we decrease the Indium flux from 0.5921 in sample 2107067 to 0.5839 in sample 2107070, the Indium content in solid phase decrases as shown in table 2.10. On increasing the Indium flux to 0.5882 in sample 2107072 again results in increased Indium content in solid phase, although the increament in Indium content in solid phase is more compared to the decreament in sample 2107070.

Table 2.10: HRXRD results for samples 2107067, 2107070 and 2107072.

Sample	**Material**	**In (x_v)**	**In (x_s)**	Mismatch ($\frac{\Delta a}{a}$) ppm
2107067	InGaAlP/GaAs	0.5921	0.4915	865
2107070	InGaAlP/GaAs	0.5839	0.4685	-829
2107072	InGaAlP/GaAs	0.5882	0.4922	821

The lattice mismatch between InGaAlP and GaAs substrate is the lowest for sample 2107072 which gives 49.22% Indium content in the solid phase. Therefore, growth condition of sample 2107072 is our optimized condition for the growth of quaternary InGaAlP waveguide material in our laser structure.

The bandgap of the InAlGaP quaternary material has been obtained by performing low temperature PL measurement of sample 2107072 at 10 K. The PL spectrum is shown in figure 2.14. The corresponding energy bandgap for the peak at wavelengths 529.5 nm is 2.34 eV at 10 K.

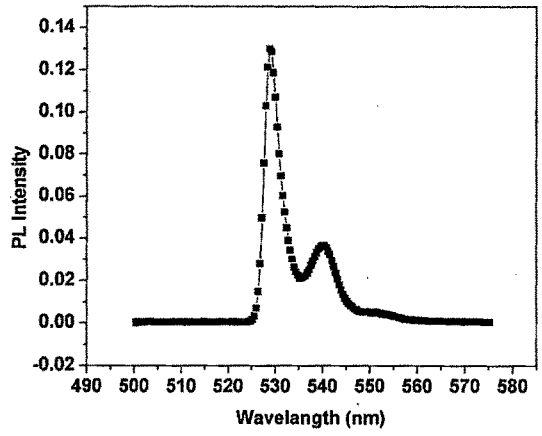

Figure 2.14: PL spectrum of sample 2107072 at low (10K) temperature.

For the calculation of composition of quaternary $In_xAl_yGa_{1-x-y}P$ from HRXRD and PL data, we have used following relation.

$$Eg_{In_xAl_yGa_{1-x-y}P} = Eg_{In_a(Al_bGa_{1-b})_{1-a}P}$$

where, we have put x = a, and y = b(1-a). So, using equation (2.21) we can write,

$$Eg_{In_xAl_yGa_{1-x-y}P} = aEg_{InP} + b(1-a)Eg_{AlP} + (1-a)(1-b)Eg_{GaP} - a(1-a)C_{InGaAlP} - b(1-a)(1-b)C_{AlGaP} \quad (2.23)$$

where, $C_{InAlGaP}$ and C_{AlGaP} are the Bowing parameters of InAlGaP and AlGaP respectively. $C_{InAlGaP} = 0.18$ and $C_{AlGaP} = 0.49$ for low temperature [6]. Thus, using these values, value of Indium contenet 'x' obtained from HRXRD, and the energy bandgap of binary end compounds at low temperature (10 K), we get the value of Aluminum content 'y' and Gallium content '1-x-y' in the quarternary compound. The summarized results of sample 2107072 are given in Table 2.11.

Table 2.11: HRXRD results for sample 2107072.

In (x)	Al (y)	Ga (1-x-y)	Corresponding bandgap (eV)	Corresponding wavelength (nm)	Compressive strain $\frac{\Delta a}{a}$ (ppm)
0.4922	0.365	0.1428	2.3399	529.5	821

2.6.3.3 InGaP QW Active Layer

After the InAlP cladding and InAlGaP waveguide layer, the next step is to optimize the growth of an InGaP QW. For the optimization of QW, two samples of InGaP QW, 2107078 and 2107079, were grown with different thickness of QW, i.e. 14 nm and 8 nm, respectively. Figure 2.15 shows the room-temperature PL spectrum for a 14 nm InGaP QW (sample 2107078). By fitting the experimental data to a Gaussian, we get the peak position to be 683.12 nm which corresponds to the energy bandgap of 1.815 eV at room temperature. The FWHM of PL curve of the sample 2107078 is about 6 nm, which shows the good quality of the QW structure.

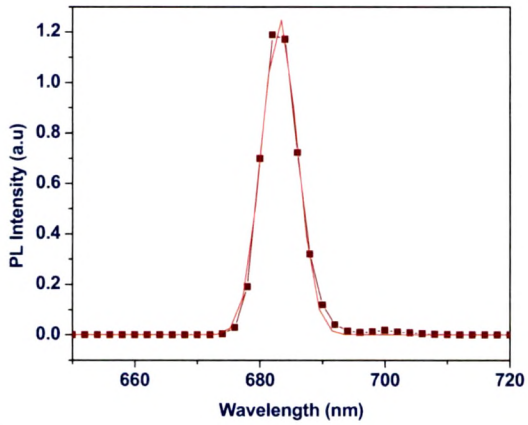

Figure 2.15: Room-temperature PL spectrum of sample 2107078.

In another sample, 2107079, the thickness of the InGaP QW is reduced in order to decrease the emission wavelength. Figure 2.16 shows the room-temperature PL spectrum for an 8 nm InGaP QW sample (2107079).

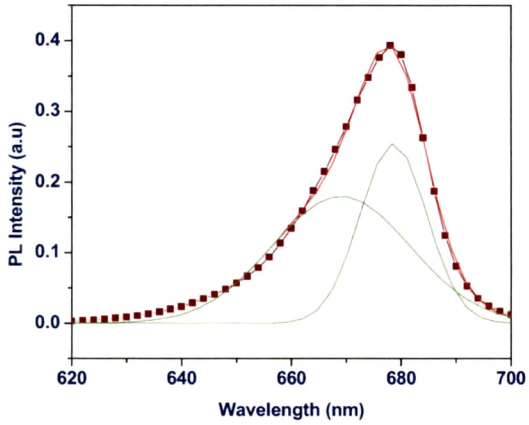

Figure 2.16: Room-temperature PL spectrum of sample 2107079.

The PL spectrum, on Gaussian fit, shows two peaks as shown in figure 2.16. The energy bandgaps corresponding to these peaks at wavelength 669 nm and 678 nm are, respectively, 1.85 eV and 1.829 eV. The FWHM of PL spectrum of the sample 2107079 is about 23 nm.

Figure 2.17 shows 10 K PL spectrum for the same sample. Again spectrum shows two Gaussian peaks. The energy bandgap corresponding to these peaks at 654 nm and 656 nm are 1.896 eV and 1.890 eV, respectively. The FWHM of PL curve of the sample 2107079 is about 7 nm, which shows the good quality of the QW structure.

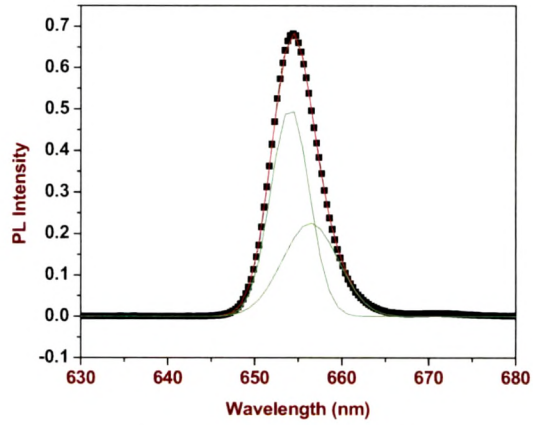

Figure 2.17: PL of sample 2107079 at low (10K) temperature.

2.6.4 Growth of a Complete Laser Structure

After optimizing individual layer parameters, complete laser structures have been grown by MOVPE technique. The two laser structures, sample 2107086 and 2107088, were grown for the fabrication of red laser diode. Both of them consist of similar layer structure and parameters except the composition of p-type InAlP cladding layer. The Indium composition in sample 2107086 is 61.5% in vapor phase (x_v) and while that in sample 2107088 is 61.1%. A 10 nm p-type InGaP layer is inserted between GaAs cap layer and p-InAlP cladding layer to provide a smoother potential for holes. This eases the hole-injection in the laser diode structure. The GaAs cap layer for these laser structures is grown at 600 °C. Figure 2.18 shows schematic of complete laser structure with growth temperatures and thickness of each layer. The energy band diagram corresponding to the laser diode structure is shown in figure 2.19.

P^+ GaAs cap layer 220nm, Tg =600 °C, carrier desity ~ $1x10^{19}$ cm^{-3}
p-InGaP 10nm, Tg= 670 °C
p-InAlP cladding layer 1000nm, Tg =700 °C, carrier desity ~$3x10^{17}$ cm^{-3}
InAlGaP waveguide layer,200nm, Tg =770 °C, undoped
InGaP (QW),8nm, Tg =670 °C
InAlGaP waveguide layer 200nm, Tg =770 °C, undoped
n-InAlP cladding layer, 1000nm, Tg= 770 °C, carrier desity ~ $1x10^{18}$ cm^{-3}
n^+- GaAs buffer, 200nm, Tg =770°C
n^+- GaAs substrate

Figure 2.18: Schematic structure for red laser diodes.

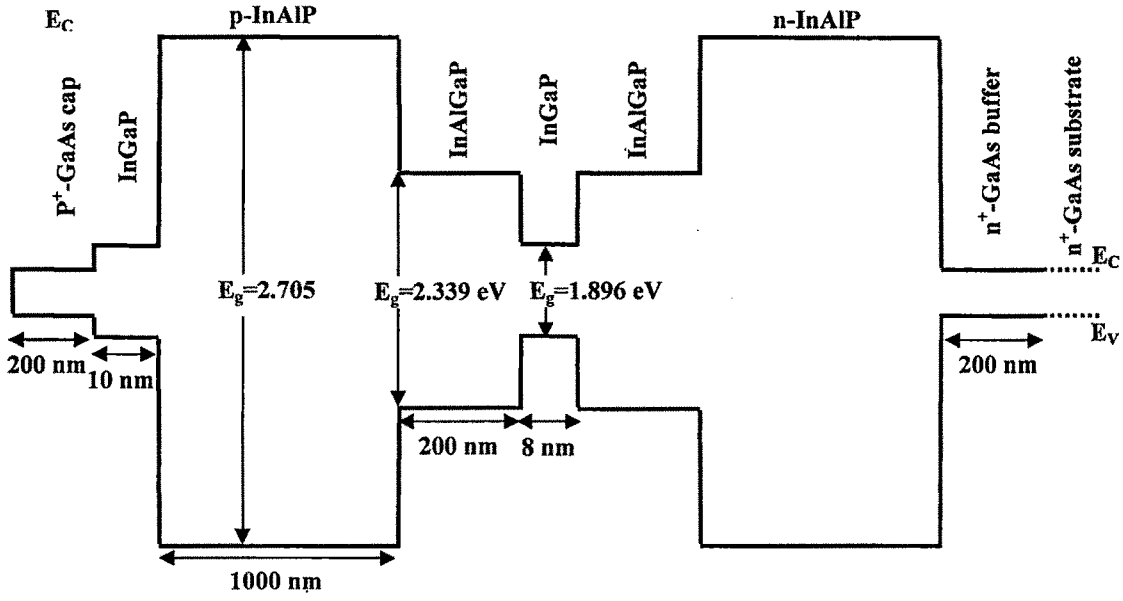

Figure 2.19: Energy band diagram for the grown laser diode structure.

Further processing and characterization of these MOVPE grown laser structures were carried out for the fabrication of red laser diode, which is described in chapter 3 in details.

➢ References

[1] G.P. Agrawal, N.K. Dutta, "*Long wavelength semiconductor lasers*", Van Nostrand Reinhold, New York, (1986)

[2] P.J.A. Thijs, L.F. Tiemeijer, J.J.M. Binsma, T.van Dogen, *IEEE J. Quant. Electron.*, **30**, pp. 477, (1994)

[3] A. Ishibashi, *IEEE J. Select. Topics Quant. Electron.*, **1**, pp. 741, (1995)

[4] S. Nakamura, G. Fasol, "*The blue laser diode*", Springer Verlag, Berlin, (1997)

[5] D. Bimberg, M. Grundmann, N. N. Ledentsov, "*Quantum Dot Heterostructures*", John Wiley & Sons, New York, (1999)

[6] Pallab Bhattacharya, "*Semiconductor Optoelectronic Devices*", pp. 21, Prentice-Hall, India, (1999)

[7] P. S. Zory, Ed; "*Quantum Well Lasers*", pp. 72, Academic Press, Boston, (1993)

[8] G. B. Stringfellow, "*Organometallic Vapor-Phase Epitaxy: Theory and Practice*", Academic Press, (1989)

[9] Z. I. Alferov, V. M. Andreev, E. L. Portnoy, M. K. Trukan, *Fiz. Tekh. Polupr.*, **3**, pp. 1328 (1969)

[10] I. Hayashi, M. B. Panish, P. W. Foy, S. Sumski, *Appl. Phys. Lett.*, **17**, pp. 109, (1970)

[11] E. A. Razeek, H. Shichijo, B. A. Vojak, N. Holonayak, Jr., *Appl. Phys. Lett.*, **31**, pp. 534, (1977)

[12] V. V. Chaldyshev, N. N. Faleev, N. A. Bert, Yu. G. Musikhin, A. E. Kunitsyn, V. V. Preobrazhenskii, M. A. Putyato, B. R. Semyagin, P Werner, *J. Cryst. Growth,* **201/202**, pp. 260, (1999)

[13] W. Patrick McCray, *Nature Nanotechnology*, **2**, pp. 259, (2007)

[14] N. Chand and R. F. Karlicek, "*Epitaxy of InGaAs*", Properties of lattice matched and strained Indium Gallium Arsenide, Ed.: Pallab Bhattacharya, pp. 221, INSPEC Publication, (1993)

[15] J. J. Coleman, *Proc. of IEEE*, **85**, pp. 1715, (1997)

[16] H. M. Manasevit, *Appl. Phys. Lett.*, **12**, 156 (1968)

[17] R.D. Dupius, P.D. Dapkus, N. Holonyak, E.A. Rezek, R.Chin, *Appl. Phys. Lett.*, **32**, pp. 295, (1978)

[18] S.D. Hersee, M. Krakowski, R. Blondeau, M. Baldy, B. De Créoux, J. P. Duchemin, *J. Cryst. Growth*, **68**, pp. 383, (1984)

[19] S.J. Bass, *J. Cryst. Growth*, **31**, pp. 172-178, (1975)

[20] R.D. Dupuis, *Jpn. J. Appl. Phys.*, **19**, **suppl. 19-1**, pp. 415, (1980)

[21] Tarun Kumar Sharma, PhD Thesis, "*Metal organic vapour phase epitaxial growth of III-V semiconductors*", pp. 7, Devi Ahilya Vishwa Vidyalaya, Indore, (2002)

[22] M. A. Tischler, *IBM J. Res. Develop.*, **34(6)**, pp. 828, (1990)

[23] D. W. Shaw, *J. Cryst. Growth,* **31**, pp. 130, (1975)

[24] D. H. Reep, S. K. Ghandhi, *J. Electrochem. Soc.*, **130(3)**, pp. 675, (1983)

[25] G. Costrini, J. J. Coleman, *J. Appl. Phys.*, **57(6)**, pp. 2249, (1985)

[26] F. C. Eversteyn, P. J. W. Severin, C. H. J. V. D. Brekel, H. L. Peek, *J. Electrochem. Soc.*, **117(7)**, pp. 925, (1970)

[27] F. Rosenberger, "*Fundamentals of Crystal Growth*", Springer, Berlin, (1979)

[28] H. Moffat, K. F. Jensen, *J. Cryst. Growth*, **77**, pp. 108, (1986)

[29] H. K. Moffat, T. F. Kuech, K. F. Jensen, P. J. Wang, *J. Cryst. Growth*, **93**, pp. 594, (1988)

[30] T. F. Kuech, M. A. Tischler, P. J. Wang, G. Scilla, R.Potemski, F. Cardone, *Appl. Phys. Lett.*, **53**, pp. 1317, (1988)

[31] P. F. Fewster, N. L. Andrew, *J. Phys. D: Appl. Phys.*, **28**, pp. A97, (1995)

[32] B.D. Cullity, "*Elements of X-Ray Diffraction*", 2nd Edn., pp. 87, Addison-Wesley, (1978)

[33] G. D. Gilliland, *Materials Science & Engineering:R*, **18(3)**, pp.99, (1997)

[34] S. M. Sze, "*Physics of Semiconductor Devices*", Wiley-Interscience, New York, (1969)

[35] P. Blood, *Semicon. Sci. Technol.*, **1(1)**, pp. 7, (1986)

[36] Eli Kapon, Ed.; "*Semiconductor Lasers II: Materials and structures*", pp. 8, Academic Press, (1999)

[37] H.B. Serreze, C.M.Harding, *Electronic Letters*, **28**, pp. 2115, (1992)

[38] Markus Weyers, Arnab Bhattacharya, Frank Bugge, Arne Knauer, "*Epitaxy of High-Power Diode Laser Structures*", High Power Diode Lasers, Ed.: R. Diehl, *Topics Appl. Phys.*, **78**, pp. 83, Springer-Verlag Berlin Heidelberg, (2000)

[39] http://www.tf.uni-kiel.de/matwis/amat/semi_en/index.html

[40] I.Vurgaftman, J.R. Meyer, L.R. Ram Mohan, *J. Appl. Phys.*, **89**, pp. 5815, (2001)

[41] H.C. Casey, M.B. Panish, "*Heterostructure Lasers B: Materials and Operating Characteristics*", Academic Press, New York, (1978)

[42] L.J. Mawst, A. Bhattacharya, J. Lopez, D. Botez, D.Z. Garbuzov, L. DeMarco, J.C. Connolly, M. Jansen, F. Fang, R. F. Nabiev, *Appl. Phys. Lett.*, **69**, pp. 1532, (1996)

[43] D W Palmer, www.semiconductors.co.uk, 2005.01e

[44] V. K. Dixit, Tapas Ganguli, S. D. Singh, S. Pal, Ravi Kumar, S. Porwal, Alexander K, T. K. Sharma, A. K. Nath, *Proc. of Sixth DAE-BRNS National Laser Symposium (NLS-6)*, Indore, India, pp.76, (2006)